FOUR DIMENSIONAL RECONSTRUCTION USING MAGNETIC INDUCTION TOMOGRAPHY: EXPERIMENTAL STUDY

H.-Y. Wei and M. Soleimani[*]

Department of Electronics and Electrical Engineering, University of Bath, UK

Abstract—Magnetic Induction Tomography (MIT) is a relatively new and emerging type of tomography techniques that is able to map the distribution of all three passive electrical properties (PEPs). Its non-invasive and contactless features make it an attractive technique for many applications compared to the traditional contact electrode based electrical impedance tomography. Recently, MIT has become a promising monitoring technique in industrial process tomography, and the area of the research interest has moved from 2D to 3D because of the volumetric nature of electromagnetic field. Three dimensional MIT images provide more information on the conductivity distribution, especially in the axial direction. However, it has been reported that the reconstructed 3D images can be distorted when the imaging object is located at a less sensitive region. Although this distortion can be compensated by adjusting the regularisation criteria, this is not practical in real life applications as the prior information about the object's location is often unavailable. This paper presents a memory efficient 4D MIT algorithm which can maintain the image quality under the same regularisation circumstances. Instead of solving each set of measurement individually, the 4D algorithm takes advantage of the correlations between the image and its neighboring data frames to reconstruct 4D of conductivity movements. The 4D algorithm improves the image qualities by increasing the temporal resolution. It also overcomes some sensitivity issues of 3D MIT algorithms and can provide a more stable result in terms of the size consistency of the reconstructed image. Several experimental results using real laboratory data are presented for validating the proposed algorithms.

1. INTRODUCTION

Magnetic induction tomography (MIT) is an electromagnetic imaging technique that images all three PEPs distribution inside a region of interest [1]. Because of its contactless feature, the entire data collection process becomes non-invasive, which makes it suitable in many applications in both industrial fields (non-destructive pipeline imaging, metal production monitoring and material inspection [2–4]) and biomedical fields [5, 6]. For a typical MIT system, coils are used as the transmitters and receivers based on the mutual inductance theory. The technique involves the inductive measurement of magnetic coupling between different coil combinations. The measured data is then manipulated using mathematical forward and inversion techniques to create an image of the distribution of the electrical properties.

In the literature, MIT have been extensively studied in 2D and most of the systems are still producing low resolution 2D imaging result [3, 4, 7–10], which focuses on the cross sectional distribution and assumes there is no axial (z-axis) conductivity variation. For some applications where the axial conductivity change is significant, this assumption is unrealistic and the 2D imaging is no longer applicable. In order to extract the variation in axial direction, 3D images are required [11–13]. 3D MIT is valuable for imaging the volumetric distribution of electrical conductivity and believed to be the future expansion trend of MIT applications. Some of the early work in 3D MIT discuss the sensitivity map calculation and inverse problem [14, 15] and has later been validated using a full scaled 3D system [16]. Like other imaging techniques [17–21], 3D MIT systems can only produce sensible results when the measured voltage difference is greater than the system noise level, i.e., adequate signal to noise ratio (SNR). A well known technique to improve SNR performance is measurement averaging, which can be applied when imaging static or slow moving objects [22]. However, in applications where the measuring target is involved with movement, the averaging technique is not appropriate as the measurements are not all taken at the same time. In this case each measurement set is no longer completely independent to each other. Averaging between the measurement sets can reduce the temporal resolution of the reconstructed images.

In this paper, we are interested in the 3D MIT reconstruction when the imaging object is moving within the measuring space. 4D images are not simply the combination of several 3D images. In the case where the movement is involved in the measurement, there are some degrees of correlation between each measurement frame. This paper

proposes a 4D temporal algorithm which extracts these correlation information to improve the noise performance and the stability over the unaveraged 3D images. In [23], Kalman filtering was proposed for temporal reconstruction in 2D MIT. The temporal algorithm proposed in this paper can be represented as an extended Kalman filtering which realise 4D temporal reconstruction in a full scale volumetric MIT system. Several 4D experiments will be demonstrated to show the advantages of the algorithm on improving the image qualities. Higher temporal resolution makes the MIT a good candidate for 4D imaging technique which can be applied into various dynamical object monitoring applications, such as molten metal flow monitoring and ice front detection for cryosurgery operation. Both of these applications require the additional information on dynamical behavior of underlying process, which can potentially be provided by the 4D algorithm presented in this paper.

2. SYSTEM SETUP

A typical three dimensional MIT system comprises multi-layer of sensor coils. Although a 3D image can also be generated by a single layer MIT system: moving the the single layer sensor array along the z-direction during the data collection process. In this case a 3-D image can be constructed by stacking up several 2-D tomographs. However, this is only applicable when the imaging target is static or very slow moving with respect to the frame rate. In order to realise the 4D temporal imaging, a multi-layer MIT system is necessary.

The MIT hardware used in this paper is the Bath Mk-II system [16], with an operational frequency of 20 kHz. The system comprises 16 channels, which are divided into two layers (8 sensor coils at each plane). The distance between the layers is 6 cm, with an cylindrical imaging area of 13 cm height and 11 cm diameter. The
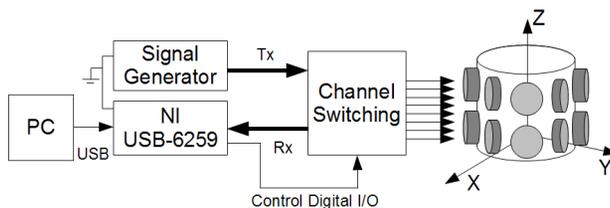
Figure 1. The system block diagram of the volumetric MIT system: Bath Mk-II.

sensor coil is a 50 turns hand wound air cored coil, which has a dimension of 4 cm diameter. These dimensions must be considered when calculating the forward problem in order to formulate a more accurate model. Figure 1 shows the system block diagram of the volumetric MIT system. With a 16 channel system, $(16 \times 15)/2 = 120$ measurements can be collected at the end of the measuring cycle.

The main disadvantage of the system is that most of the image processing time was spent at the data acquisition. At this stage the Mk-II system takes 4 seconds to complete 120 measurements, i.e., the image can only be updated at a rate of 0.25 frame/sec. To encounter this, the speed of the moving objects in the experiments need to slow down to match the system frame rate.

3. EDDY CURRENT MODELING

The forward problem in MIT is the simulation of the measurement data for a given conductivity distribution and excitation signal. The forward problem needs to be solved in order to obtain the sensitivity map for the later image reconstruction task. The forward problem of MIT is a general eddy current problem, where the magnetic vector potential (A) needs to be simulated using Maxwell equations [14, 24]. Validation of the forward model has been done in a previous study. Under a quasi-static approximation, given that

$$E = -i\omega A \tag{1}$$

and

$$B = \nabla \times A, \tag{2}$$

we can obtain the following equation:

$$\nabla \times \left(\mu^{-1}\nabla \times A\right) + i\omega\sigma A = J_s, \tag{3}$$

where μ is the electrical permeability, σ the electrical conductivity, and ω the angular frequency. Equation (3) is a differential form of the eddy current problem. Alternatively, we can solve the problem using its integration form by implementing the Biot-Savart Law, which is used to define the magnetic field at each mesh element [24–26]

$$B = \int \frac{\mu_0}{4\pi} \frac{Idl \times r}{|r|^3}, \tag{4}$$

where I is the source current, dl a vector whose magnitude is the length of the differential element of the wire, μ_0 the vacuum permeability constant, and B the integration of the magnetic field along each source current segment. This magnetic vector potential A is defined based on the system dimension we described in the previous section. A

simple grid mesh was implemented into the forward model, with no complicated discretisation of sensor coils.

When the forward model is solved, the sensitivity map, also known as Jacobian matrix, can then be defined. The sensitivity term for each element we defined in the system is

$$\frac{\delta V_{ij}}{\delta \sigma_k} = -\frac{\omega^2}{I_i I_j} \int\limits_{\Omega_{ek}} \{A_i\} \cdot \{A_j\} dv. \tag{5}$$

Equation (5) gives us sensitivity of the induced voltage pairs V_{ij} of coils of i, j with respect to an element. Ω_{ek} is the volume of element number k, I_i and I_j are excitation currents for the sensor i and sensor j respectively. Each row of the Jacobian matrix will be sensitivity of a given measured voltage over the changes in conductivity distribution.

4. 4D IMAGE RECONSTRUCTION

4.1. Inverse Problem

The inverse problem for MIT is to convert the voltage measurements into a conductivity distribution image. The inverse problem in MIT is generally ill-posed and non-linear. However, solving a non-linear problem requires extensive computation of electromagnetic fields and updating the sensitivity maps [27]. Therefore, in most of the electrical tomography cases, linear responses are often presumed when reconstructing images using inverse solvers. This linear response assumption can simplify the non-linear problem to a linear approximation, where the problem can be solved through the matrix multiplications.

Given a linear response equation $\mathbf{Kf} = \mathbf{b}$, where $\mathbf{K}$ is the Jacobian matrix with size $m \times n$, $\mathbf{f}$ is the conductivity distribution and $\mathbf{b}$ is the normalised sensor measurement, the single step Gauss Newton inverse solver with Tikhonov regularisation is to find the solution $\mathbf{f}$ which has the minimum error function:

$$\|\mathbf{b} - \mathbf{Kf}\|_2^2 + \|\mathbf{f} - \mathbf{f}_0\|_2^2. \tag{6}$$

If $\mathbf{f}_0$ is set to 0, the linear algebra in Equation (6) can be rearranged to the following form

$$\mathbf{f} = \left(\mathbf{K}^\top \mathbf{K} + \lambda \mathbf{R}\right)^{-1} \mathbf{K}^\top b, \tag{7}$$

where $\mathbf{R}$ is the weighting matrix and λ the Tikhonov regularisation parameter. Choosing λ properly can effectively increase the system stability and remove the sharp edge from the reconstruction images, which results in a stable reconstructed object with smooth surface.

The main challenge with this type of inverse technique (Equation (6)), especially in a large scaled 3D problem, is that a tremendous amount of memory is required to solve the $\mathbf{K}^\top\mathbf{K}$ and its inversion calculation. Since in most of the 3D cases, the number of columns n in matrix $\mathbf{K}$ is too large to compute when solving the inverse problem, some alternative inverse methods are required to resolve the limited memory issue [22, 28]. Equation (6) can be rewritten as:

$$\mathbf{f}=\left[\left(\mathbf{K}^\top\mathbf{K}+\lambda\mathbf{R}\right)^{-1}\mathbf{K}^\top\left(\mathbf{K}\frac{1}{\lambda}\mathbf{P}\mathbf{K}^\top+\mathbf{I}\right)\left(\mathbf{K}\frac{1}{\lambda}\mathbf{P}\mathbf{K}^\top+\mathbf{I}\right)^{-1}\right]\mathbf{b}$$

$$=\left[\left(\mathbf{K}^\top\mathbf{K}+\lambda\mathbf{R}\right)^{-1}\left(\mathbf{K}^\top\mathbf{K}+\lambda\frac{1}{\mathbf{P}}\right)\left(\frac{1}{\lambda}\mathbf{P}\mathbf{K}^\top\right)\left(\mathbf{K}\frac{1}{\lambda}\mathbf{P}\mathbf{K}^\top+\mathbf{I}\right)^{-1}\right]\mathbf{b}$$

$$=\left(\mathbf{P}\mathbf{K}^\top\right)\left(\mathbf{K}\mathbf{P}\mathbf{K}^\top+\lambda\mathbf{I}\right)^{-1}\mathbf{b}, \tag{8}$$

where $\mathbf{P}=\mathbf{R}^{-1}$ and $\mathbf{R}$ is the regularisation matrix that represents the spatial correlation between imaging pixels. $\mathbf{R}$ is usually the identity matrix in MIT. Using Equation (8), the $\mathbf{K}^\top\mathbf{K}$ multiplication can be avoided, hence the memory size and the computational time required for solving the inversion can be reduced dramatically. For a three dimensional $17\times17\times17$ grid mesh, Equations (7) and (8) require 4.99 seconds and 0.03 second respectively for solving the same linear equation (Intel T7700 Core2Duo 2.4 GHz CPU). Using Equation (8) can effectively increase the time efficiency by a factor 160. Please note that Equation (8) does not consider any temporal information in the reconstructed data. Each data frame is still solved independently with no correlation involved.

4.2. Temporal Solver

Instead of using the Kalman filtering, which the image is reconstructed based on the current data and the past image frames [23], the 4D algorithm we implement uses the neighboring data set which are nearby in time to estimate the reconstructed image [22]. Figure 2 shows a simple illustration of 4D MIT image reconstruction. Each time frame corresponds to a 3D image using Equation (8), and each 4D image is reconstructed based on the correlation between several 3D images.

Reconstructing one 4D image requires multiple 3D image frames. If a sequence of the 3D measurement sets are obtained within a time period from t_{-d} to t_d, the total measurement sets can be formulated as

$$\tilde{\mathbf{b}}=[\mathbf{b}_{-d},\mathbf{b}_{-d+1},\ldots,\mathbf{b}_{d-1},\mathbf{b}_d] \tag{9}$$
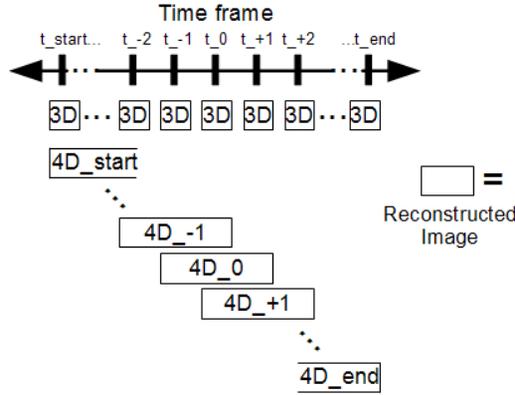
Figure 2. Illustration of 4D image reconstruction ($d = 1$), each of the 4D image is reconstructed by $2d + 1$ frames of 3D images.

and the corresponding conductivity distribution is

$$\tilde{\mathbf{f}} = [\mathbf{f}_{-d}, \mathbf{f}_{-d+1}, \ldots, \mathbf{f}_{d-1}, \mathbf{f}_d]. \tag{10}$$

Given a linear forward model $\mathbf{b} = \mathbf{Kf}$, all the models within the time frame can be concatenated into the following form

$$
\begin{bmatrix}
\mathbf{b}_{-d} \\
\mathbf{b}_{-d+1} \\
\vdots \\
\mathbf{b}_{d-1} \\
\mathbf{b}_d
\end{bmatrix}
=
\begin{bmatrix}
\mathbf{K} & 0 & \cdots & & 0 \\
0 & \ddots & & & \\
\vdots & & \mathbf{K} & & \vdots \\
& & & \ddots & 0 \\
0 & & \cdots & 0 & \mathbf{K}
\end{bmatrix}
\begin{bmatrix}
\mathbf{f}_{-d} \\
\mathbf{f}_{-d+1} \\
\vdots \\
\mathbf{f}_{d-1} \\
\mathbf{f}_d
\end{bmatrix}
\tag{11}
$$

and also as

$$\tilde{\mathbf{b}} = \tilde{\mathbf{K}}\tilde{\mathbf{f}}, \tag{12}$$

where $\mathbf{K}$ is the Jacobian matrix, which is assumed to be a constant during the time frame. The concatenated Jacobian matrix $\tilde{\mathbf{K}}$ is $\mathbf{I} \otimes \mathbf{K}$, where the identity matrix has a size of $2d + 1$. The $\otimes$ notation is the Kronecker product, which results in $\tilde{\mathbf{K}}$ as a block diagonal matrix.

In the temporal algorithm, the conductivity estimation at time t_0 is calculated from the data set within the time frame from t_{-d} to t_d. The correlation corresponding elements between adjacent frames can be represented by an inter-frame correlation coefficient γ, which has a range from 0 (independent) to 1 (fully dependent). As the time difference between each frame increases, γ becomes closer to 0 as the correlation decreases between the adjacent measurements. Frames with

large time lag can be considered independent. The inversion equation
with Tikhonov regularisation (Equation (8)) can be re-written as

$$\tilde{\mathbf{f}} = \left(\tilde{\mathbf{P}}\tilde{\mathbf{K}}^\top\right)\left(\tilde{\mathbf{K}}\tilde{\mathbf{P}}\tilde{\mathbf{K}}^\top + \lambda\tilde{\mathbf{W}}^{-1}\right)^{-1}\tilde{\mathbf{b}}, \qquad (13)$$

where $\tilde{\mathbf{W}} = \mathbf{I} \otimes \mathbf{W}$ and $\mathbf{W}$ is the regularisation matrix for the
measurement noise. $\mathbf{W}$ is modeled as identity matrix since the
measurement noise between frames are assumed independent. λ here
again is the regularisation parameter. $\tilde{\mathbf{P}} = \mathbf{T} \otimes \mathbf{P}$ where $\mathbf{T}$ is the
regularisation matrix that represents the temporal correlation between
the sequential images. The size of the $\mathbf{T}$ is determined by the time step
d and is defined as follows:

$$\mathbf{T} = \begin{bmatrix} 1 & \gamma & \cdots & \gamma^{2d-1} & \gamma^{2d} \\ \gamma & 1 & \cdots & \gamma^{2d-2} & \gamma^{2d-1} \\ \vdots & \vdots & \ddots & \vdots & \vdots \\ \gamma^{2d-1} & \gamma^{2d-2} & \cdots & 1 & \gamma \\ \gamma^{2d} & \gamma^{2d-1} & \cdots & \gamma & 1 \end{bmatrix}. \qquad (14)$$

From Equations (13) and (14), we can obtain

$$\tilde{\mathbf{f}} = \left[\mathbf{T} \otimes \left(\mathbf{P}\mathbf{K}^\top\right)\right]\left[\mathbf{T} \otimes \left(\mathbf{K}\mathbf{P}\mathbf{K}^\top\right) + \lambda\left(\mathbf{I} \otimes \mathbf{W}^{-1}\right)\right]^{-1}\tilde{\mathbf{b}}, \qquad (15)$$

where the temporal reconstructed result $\tilde{\mathbf{f}}$ has the following form:

$$\begin{bmatrix} \tilde{\sigma}_{-d} \\ \vdots \\ \tilde{\sigma}_0 \\ \vdots \\ \tilde{\sigma}_d \end{bmatrix} = \tilde{\mathbf{f}}. \qquad (16)$$

Although this reconstruction result is an augmented image
sequence, typically only the current conductivity distribution $\tilde{\sigma}_0$ is
interested and will be used as the reconstructed 4D image result.
In reality, Both $\tilde{\mathbf{b}}$ (acquired by real system) and $\tilde{\mathbf{K}}$ (FEM model of
the forward problem) contribute error and noise to the inverse solver.
However it is shown that in a noisier data, the 4D algorithm actually
outperforms the 3D algorithm [29].

5. EXPERIMENTAL RESULTS

In order to evaluate the performance of proposed 4D method in
comparison with to the traditional single step 3D method, several
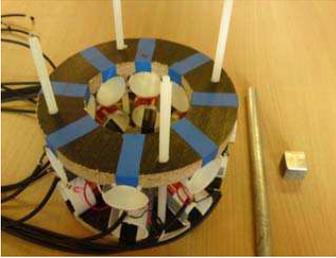
Figure 3. Bath Mk-II system and the sample objects used in the experiments.
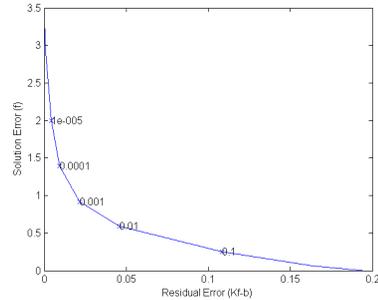
Figure 4. The L curve plot used for choosing regularisation factor.

laboratory based experiments were conducted using the Bath Mk-II system. A 2.4 cm metallic iron cube and a 20 cm long aluminum rod were used as imaging targets (Figure 3) Each object was moved into the system imaging area under different angles and movement directions. All the results shown in Figures 5 and 6 are the comparison between the reconstructed 3D and 4D images. The regularisation parameter was chosen based on the L-curve method (Figure 4) and then empirically checked for a wide range of parameters near the ideal value. A safer choice of 0.1 regularisation factor was selected, due to the fact of limited measurement for volumetric imaging. A larger regularisation factor can make the reconstructed images more stable and noise-resistant. The temporal correlation coefficient γ and the time step d were chosen to be 0.5 and 1 respectively for temporal reconstructions. All the object movements in the experiments were well matched according to the frame rate of the MIT system.

In the first two experiments a moving steel cube was used to evaluate the performance of the temporal algorithms. Figure 5(a) shows the experimental result when the metallic cube was moving vertically downwards with an estimated speed of 2.5 mm/sec into the central area of the imaging region. Figure 5(b) shows the result under the same movement speed but different path orientations; the metallic cube was moved diagonally across the imaging region.
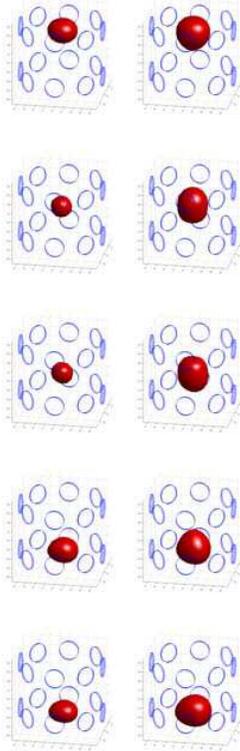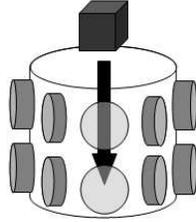
In all cases, the 4D algorithms successfully reconstructed the sample movement from the 3D results. To achieve a better noise performance, all the images shown here are the thresholded result from the reconstructed images. In electrical tomography, it is known that the centre of the imaging area always has a weaker sensitivity, since the region is more distant from the coil sensors. With the same
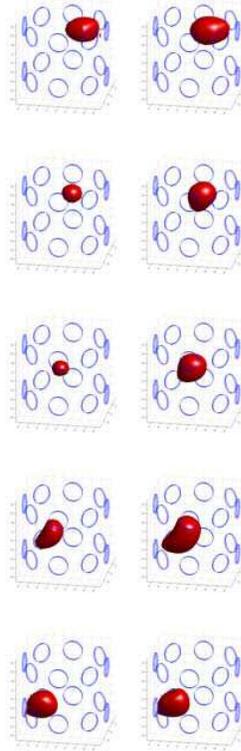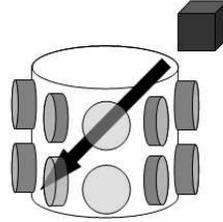
Figure 5. Comparison between 3D and 4D MIT visualisation of a moving metallic cube which move (a) vertically downwards and (b) diagonally downwards.

Figure 6. Comparison between 3D and 4D MIT visualisation of a moving aluminum rod.

regularisation factor, the shape of the reconstructed image can be distorted during the moving process depending on the object's location. In the experimental results shown in Figure 5, the reconstructed size of the 3D imaging object was observed to be smaller when the steel cube was moved to the central area of low sensitivity. Here the advantages of using the 4D algorithms could be seen. Aside from the successful temporal 4D reconstruction, the size of the reconstructed object was considered to be much more consistent throughout the entire movement process. When the steel cube was moved through the centre region, the difference in size of the imaged steel cube when placed in the central region is negligible in 4D images. These results indicate that 4D imaging can provide animations/images with a better stability in terms of the shape consistency.

During the first two experiments the steel cube with 2.4 cm side length was used. To further verify our hypothesis that 4D algorithms can overcome the the issue of poor sensitivity and enhance the image stability, another experiment was performed using the aluminum rod. This time the rod was inserted vertically downwards near the wall of the imaging area, also under an estimated speed of 2.5 mm/sec. In the previous 3D literature [16], it is known that the area around the side wall and between the horizontal sensor layers also has a low sensitivity, due to the nature of the electromagnetic field distribution. Less shape distortion is expected in the image in the reconstructed 4D images if the hypothesis is correct. Figure 6 shows the results of the rod experiment, which compares the reconstruction/visualisation of the 3D and 4D MIT methods.

As stated previously, MIT has a limited resolution due to the nature of the soft-field tomography. All the 3D/4D results for the experiments were visualised in the contour manner as it can best highlight the central aspect of this paper in terms of the improvement on shape preservation. The results from the rod experiment are also promising. In both cases shown in Figure 6, the movement of the object were reconstructed successfully; the rod shape is clear in the final frame of both the 3D and 4D sequences. However, the shape of the reconstructed object started to be distorted when the rod was moved into the low sensitivity area (starting from the 4th frame), i.e., the regions near the side wall and in between the sensor layers. One can see that the size of the reconstructed rod in the images were again decreased when the aluminum rod entered the insensitive region. In contrast, the size distortion phenomenon is shown to be less severe in the 4D images. It is worth noting that if the 3D images were reconstructed individually, the shape distortion problem could be rectified by adjusting the regularisation factor when solving the inverse

problem. However, this can only be realised if the information of the object location/moving path can be obtained in advanced, which is unrealistic for most of the applications. With no prior knowledge, the regularisation factor must be consistent during the entire image reconstruction process. Under the same regularisation, it is shown that the temporal correlation algorithm can effectively image the object movement with a better stability (size consistency) regardless of the poor sensitivity.

6. CONCLUSION

A 4D temporal image reconstruction has been demonstrated using MIT for the first time. By extracting the correlation information between the 3D data frames, the 4D conductivity distribution can be reconstructed. It is demonstrated that implementing the temporal correlation can improve not only the temporal resolution of the images, but also the spatial resolution in terms of the image stability. The 4D algorithm can correctly reconstruct the movement of the object, and the size of the reconstructed object will not be altered due to the inconsistency of the sensitivity distribution within the imaging volume. The implementation of the 4D algorithms is promising and can be applied into many MIT applications which involves the movement of imaging samples. In 4D reconstruction, the temporal correlation coefficient γ needs to be decided based on the frame rate of the imaging system and the movement speed of the imaging target. The main 'bottleneck' of the experiments presented in this paper is the slow frame rate of the system. To demonstrate the performance of the 4D algorithms, the metallic object was moved under a relatively slow speed. With a faster data acquisition system, the experiments can be performed at a faster pace, which would probably be more realistic in terms of the real life applications. However, the aim of this paper is to demonstrate the feasibility of applying the 4D algorithms into MIT techniques. Improving the system frame rate is beyond the scope of this paper and will be addressed in future work. Under the same regularisation factor throughout the entire moving process, the obtained 4D results have more consistency in terms of shape reconstruction. If a prior knowledge of the temporal change of the conductivity distribution is known (which is often available in the physical model of a real application), then the selection of the the optimal γ can be done in a more reasonable way. The 4D algorithm expand the previous Kalman filter based temporal algorithms to a complete 4D MIT imaging system. By introducing an explicit control over the regularisation factor and the weighted time correlation

coefficient, the image can be reconstructed successfully, even the imaging object is moving under high speed around the insensitive region in the measuring space.

REFERENCES

1. Soleimani, M., "Simultaneous reconstruction of permeability and conductivity in magnetic induction tomography," *Journal of Electromagnetic Waves and Applications*, Vol. 23, Nos. 5–6, 785–798, 2009.

2. Peyton, A. J., Z. Z. Yu, S. Al-Zeibak, N. H. Saunders, and A. R. Borges, "Electromagnetic imaging using mutual inductance tomography: Potential for process applications," *Particle & Particle Systems Characterization*, Vol. 12, No. 2, 68–74, Apr. 1995.

3. Ma, X., S. R. Higson, A. Lyons, and A. J. Peyton, "Development of a fast electromagnetic induction tomography system for metal process applications," *Proc. 4th World Congress on Industrial Process Tomography, WCIPT4*, 196–201, Aizu, Japan, Sep. 2005.

4. Ma, X., A. J. Peyton, S. R. Higson, A. Lyons, and S. J. Dickinson, "Hardware and software design for an electromagnetic induction tomography (EMT) system applied to high contrast metal process applications," *Meas. Sci. Technol.*, Vol. 17, No. 1, 111–118, 2006.

5. Watson, S., R. J. Williams, W. A. Gough, and H. Griffiths, "A magnetic induction tomography system for samples with conductivities less than $10\,\text{s·m}^{-1}$," *Meas. Sci. Technol.*, Vol. 19, 045501, 2008.

6. Scharfetter, H., R. Casanas, and J. Rosell, "Biological tissue characterization by magnetic induction spectroscopy (MIS): Requirements and limitations," *IEEE Transactions on Biomedical Engineering*, Vol. 50, No. 7, 870–880, Jun. 2003.

7. Vauhkonen, M., M. Hamsch, and C. H. Igney, "A measurement system and image reconstruction in magnetic induction tomography," *Physiol. Meas.*, Vol. 29, S445–S454, 2008.

8. Merwa, R., K. Hollaus, P. Brunner, and H. Scharfetter, "Solution of the inverse problem of magnetic induction tomography (MIT)," *Physiol. Meas.*, Vol. 26, S241–S250, 2005.

9. Watson, S., R. J. Williams, H. Griffiths, W. Gough, and A. Morris, "Magnetic induction tomography: Phase versus vector-voltmeter measurement techniques," *Physiol. Meas.*, Vol. 24, 555–564, 2003.

10. Korjenevsky, A. V. and V. A. Cherepenin, "Progress in realization

of magnetic induction tomography," *Annals of the New York Academy of Sciences*, Vol. 873, 346–352, 1999.

11. Banasiak, R., Z. Ye, and M. Soleimani, "Improving three-dimensional electrical capacitance tomography imaging using approximation error model theory," *Journal of Electromagnetic Waves and Applications*, Vol. 26, Nos. 2–3, 411–421, 2012.

12. Solimene, R., A. Brancaccio, R. Di Napoli, and R. Pierri, "3D sliced tomographic inverse scattering experimental results," *Progress In Electromagnetics Research*, Vol. 105, 1–13, 2010.

13. Goharian, M., M. Soleimani, and G. R. Moran, "A trust region subproblem for 3D electrical impedance tomography inverse problem using experimental data," *Progress In Electromagnetics Research*, Vol. 94, 19–32, 2009.

14. Soleimani, M., "Sensitivity maps in three-dimensional magnetic induction tomography," *Insight*, Vol. 48, No. 1, 39–44, Jan. 2006.

15. Soleimani, M., W. R. B. Lionheart, A. J. Peyton, X. Ma, and S. R. Higson, "A three-dimensional inverse finite-element method applied to experimental eddy-current imaging data," *IEEE Transactions on Magnetics*, Vol. 42, 1560–1567, May 2006.

16. Wei, H.-Y., L. Ma, and M. Soleimani, "Volumetric magnetic induction tomography," *Meas. Sci. Technol.*, Vol. 23, No. 5, 055401, 2012.

17. Flores-Tapia, D., M. O'Halloran, and S. Pistorius, "A bimodal reconstruction method for breast cancer imaging," *Progress In Electromagnetics Research*, Vol. 118, 461–486, 2011.

18. Liao, K.-F., X.-L. Zhang, and J. Shi, "Fast 3-D microwave imaging method based on subaperture approximation," *Progress In Electromagnetics Research*, Vol. 126, 333–353, 2012.

19. Qi, Y., W. Tan, Y. Wang, W. Hong, and Y. Wu, "3D bistatic omega-K imaging algorithm for near range microwave imaging systems with bistatic planar scanning geometry," *Progress In Electromagnetics Research*, Vol. 121, 409–431, 2011.

20. Catapano, I., F. Soldovieri, and L. Crocco, "On the feasibility of the linear sampling method for 3D GPR surveys," *Progress In Electromagnetics Research*, Vol. 118, 185–203, 2011.

21. Asimakis, N. P., I. S. Karanasiou, and N. K. Uzunoglu, "Non-invasive microwave radiometric system for intracranial applications: A study using the conformal L-notch microstrip patch antenna," *Progress In Electromagnetics Research*, Vol. 117, 83–101, 2011.

22. Adler, A., T. Dai, and W. R. B. Lionheart, "Temporal image

reconstruction in electrical impedance tomography," *Physiol. Meas.*, Vol. 28, S1–S11, 2007.

23. Soleimani, M., "Improving the temporal resolution of magnetic induction tomography for molten metal flow visualization," *IEEE Transactions on Instrumentation and Measurement*, Vol. 59, No. 3, 553–557, 2010.

24. Biro, O., "Edge element formulations of eddy current problems," *Comput. Methods Appl. Mech. Engrg.*, Vol. 169, 391–405, 1999.

25. Biro, O. and J. Preis, "On the use of the magnetic vector potential in the finite element analysis of three-dimensional eddy currents," *IEEE Transaction on Magnetics*, Vol. 25, No. 4, 3145–1359, 1989.

26. Kameari, A., "Regularization on ill-posed source terns in FEM computation using two magnetic vector potentials," *IEEE Transaction on Magnetics*, Vol. 40, No. 2, 1310–1313, 2004.

27. Banasiak, R., R. Wajman, D. Sankowski, and M. Soleimani, "Three-dimensional nonlinear inversion of electrical capacitance tomography data using a complete sensor model," *Progress In Electromagnetics Research*, Vol. 100, 219–234, 2010.

28. Wei, H.-Y. and M. Soleimani, "Three dimensional magnetic induction tomography imaging using a matrix free Krylov subspace inversion algorithm," *Progress In Electromagnetics Research*, Vol. 122, 29–45, 2012.

29. Soleimani, M., C. N. Mitchell, R. Banasiak, R. Wajman, and A. Adler, "Four-dimensional electrical capacitance tomography imaging using experimental data," *Progress In Electromagnetics Research*, Vol. 90, 171–186, 2009.